Journal of Materials Chemistry

www.rsc.org/materials

Volume 21 | Number 31 | 21 August 2011 | Pages 11441–11652

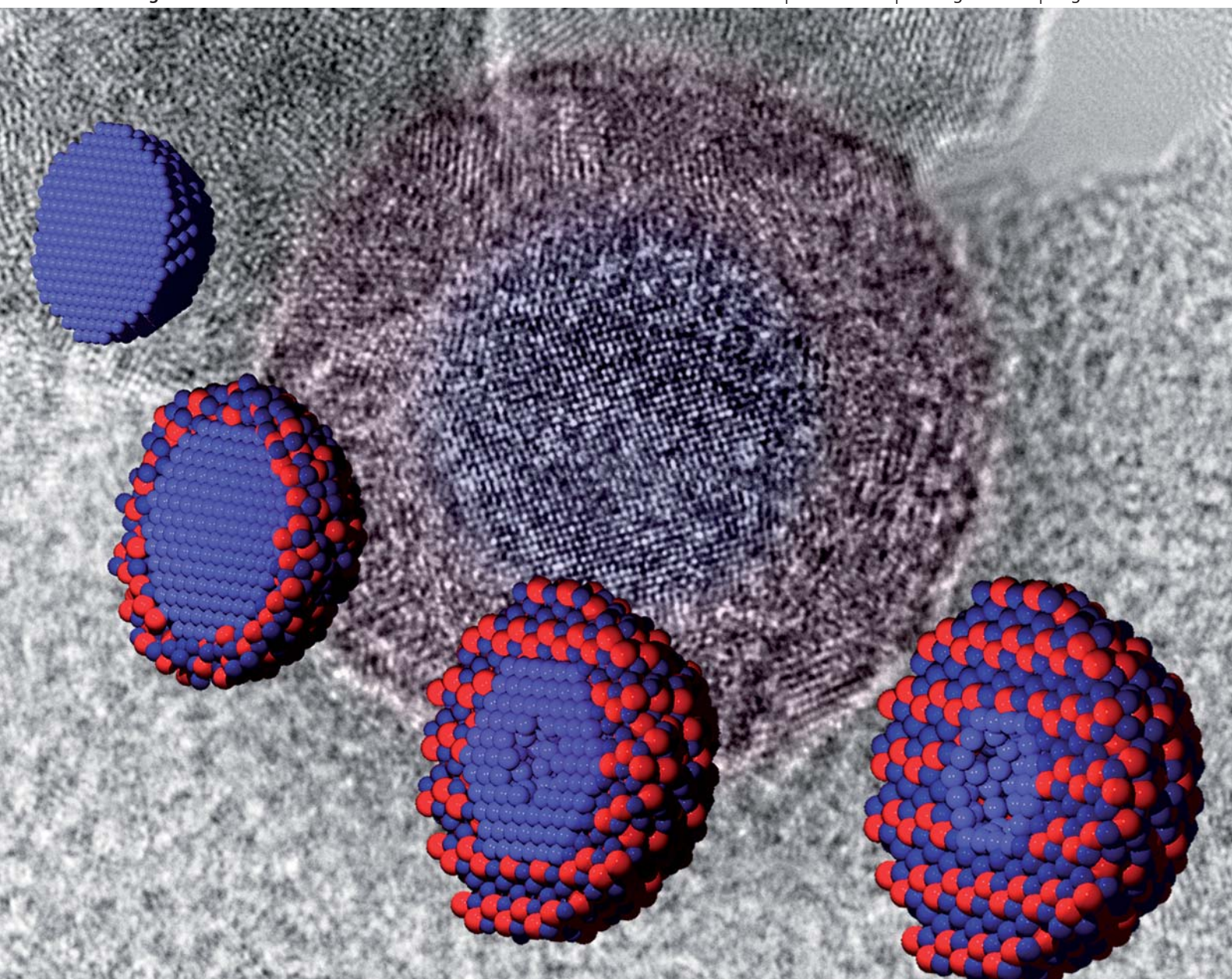

Themed issue: Chemical Transformations of Nanoparticles

ISSN 0959-9428

RSC Publishing

PAPER

Richard D. Robinson *et al.*

The structural evolution and diffusion during the chemical transformation from cobalt to cobalt phosphide nanoparticles

Journal of Materials Chemistry

Dynamic Article Links

Cite this: *J. Mater. Chem.*, 2011, **21**, 11498

www.rsc.org/materials

PAPER

The structural evolution and diffusion during the chemical transformation from cobalt to cobalt phosphide nanoparticles†

Don-Hyung Ha, Liane M. Moreau, Clive R. Bealing, Haitao Zhang, Richard G. Hennig and Richard D. Robinson*

Received 21st January 2011, Accepted 20th March 2011
DOI: 10.1039/c1jm10337g

We report the structural evolution and the diffusion processes which occur during the phase transformation of nanoparticles (NPs), ε-Co to Co_2P to CoP, from a reaction with tri-n-octylphosphine (TOP). Extended X-ray absorption fine structure (EXAFS) investigations were used to elucidate the changes in the local structure of cobalt atoms which occur as the chemical transformation progresses. The lack of long-range order, spread in interatomic distances, and overall increase in mean-square disorder compared with bulk structure reveal the decrease in the NP's structural order compared with bulk structure, which contributes to their deviation from bulk-like behavior. Results from EXAFS show both the Co_2P and CoP phases contain excess Co. Results from EXAFS, transmission electron microscopy, X-ray diffraction, and density functional theory calculations reveal that the inward diffusion of phosphorus is more favorable at the beginning of the transformation from ε-Co to Co_2P by forming an amorphous Co-P shell, while retaining a crystalline cobalt core. When the major phase of the sample turns to Co_2P, the diffusion processes reverse and cobalt atom out-diffusion is favored, leaving a hollow void, characteristic of the nanoscale Kirkendall effect. For the transformation from Co_2P to CoP theory predicts an outward diffusion of cobalt while the anion lattice remains intact. In real samples, however, the Co-rich nanoparticles continue Kirkendall hollowing. Knowledge about the transformation method and structural properties provides a means to tailor the synthesis and composition of the NPs to facilitate their use in applications.

Complexity is an emerging and important area for chemical research.[1] Just as living systems have adapted by demonstrating a hierarchical organization of structure and function over many length scales, materials can display very different properties depending on their length scale. While bulk materials are generally well understood and characterization methods to study them are mature, materials on the nanoscale can display complex behavior due to the emergence of novel and non-bulk properties that result from their small size.

Chemical transformations in bulk systems follow pathways that can be described by standard thermochemical kinetic models. Nanoscale systems, however, can display interesting and unpredictable transformation kinetics that increase the structural complexity of the original material.[2–11] Characterization of the transformation routes to form the complex final structure is one of the major challenges in nanoscience. A more complete understanding of the transformation pathways would enable the prediction of the unique products resulting from chemical transformations of nanoparticles.

Structural characterization of nanoparticles is a multifaceted problem. Nanoscale materials present a challenge to both experimental and theoretical methods due to their small size and the importance of their surfaces. The finite size of nanoparticles creates broadened features in the experimental data from typical characterization tools, blurring distinctions between the features. In addition, the high surface to volume ratio places greater emphasis on knowing the structure of the surface and near-surface layers, which are difficult to characterize. For theoretical methods it is the lack of translational symmetry and the importance of the surfaces that complicate the study of nanoparticles. A combination of experimental and theoretical methods can overcome these problems and enable the determination of atomic ordering, kinetic changes and structural aspects of nanoparticles. Experimental methods based on X-rays and electron microscopy can provide important structural information. Computational studies such as density functional theory (DFT) calculations can provide information about the energetics and atomistic structures of surfaces and diffusion barriers.

X-Ray absorption spectroscopy (XAS) is a powerful and versatile means to study structures of materials. When combined

Department of Materials Science and Engineering, Cornell University, Ithaca, NY, 14853, USA. E-mail: rdr82@cornell.edu

† Electronic supplementary information (ESI) available. See DOI: 10.1039/c1jm10337g

with other tools such as X-ray diffraction (XRD) and transmission electron microscopy (TEM), a nearly complete structural and morphological picture of a nanoparticle sample can be assembled. EXAFS measures real-space structural information, probing local range (within ~8 Å) around a central atom (in our case cobalt), and determining the partial radial distribution of atoms which are neighbors to the central atom.[12,13] EXAFS and XRD are complementary techniques: EXAFS probes local structure about a central atom while XRD reports long-range order.

EXAFS is a useful tool for probing the structural properties of nanoparticles.[13,14] Multiple-scattering path degeneracies can be reliably extracted from nanoparticle EXAFS data to yield information on size, shape, coordination number of the first shell, and surface orientation of nanoclusters.[1,12,15] Surface structure and coordination number at the surface can be determined for nanoparticles if the interior is assumed to have bulk-like coordination values.[15,16] EXAFS has been used successfully to characterize structures in nanoparticle metal and bi-metallic clusters made through gas-phase synthesis on supports,[11,17–20] and metal and semiconductor nanoparticles made through solution-phase chemistry.[15,16,21–25]

The use of EXAFS to characterize chemical transformations in nanoparticles (NPs) is relatively rare. One study related to our work used EXAFS to characterize CoPt core–shell nanoparticles formed from a chemical transformation of Co metal NPs.[21] In that study, the nanoparticle Co metal core is partially oxidized and the Pt ion is reduced (due to the favorable redox potential) on the core's surface to form the shell. Characterization of the core–shell nanoparticles was performed, however, only on fully-transformed samples of $Co_{core}Pt_{shell}$ nanoparticles. No attempt to document the intermediate stages was reported, therefore the information about the chemical transformation mechanism in this report is limited.

The precise structural characterization and understanding of chemical transformations in nanoparticles is not well understood. This is due partly to the lack of well-defined model systems and difficulties in characterization. We have chosen the cobalt phosphide system as a model system to investigate this topic. Here we report on the chemical transformation of nanoparticle ε-Co metal into two phases of cobalt phosphide, Co_2P and CoP, studied through a combined analytical effort involving EXAFS, XRD, TEM, SQUID, and DFT. In this study the nanoparticles of Co metal are transformed to cobalt phosphide phases by the addition of tri-n-octylphosphine (TOP) (Fig. 1). The nanoparticle Co metal core is reacted with TOP to successively transform the nanoparticle into Co_2P and then CoP. Six samples are prepared that represent different stages of this transformation: samples are arrested during sequential reaction stages and cleaned and prepared for analysis.

Metal phosphides are particularly interesting materials due to their wide range of unique properties including ferromagnetism, superconductivity, catalytic activity, magnetoresistance, and magnetocaloric effects.[26–29] Cobalt phosphides have recently received increased attention due to their catalytic and magnetic properties as well as their potential as a promising anode material.[30–34] Recently, we have reported a controlled synthesis of hyperbranched Co_2P using tri-n-octylphosphine oxide (TOPO) as a phosphorus source.[35] Previously reported syntheses of cobalt phosphides, however, displayed a lack of pure phase control mainly due to having multiple energetically favorable stoichiometries.[36,37] The changes in nanoparticle properties during this phase transition also remained unknown, which inhibits improvement of the synthesis and functionalization of these promising nanostructures.

In particular, in the cobalt to cobalt phosphide transformation reaction we seek to understand: (1) kinetics of the nanoscale Kirkendall transformation, (2) diffusion processes during chemical conversion, (3) shell growth through the nanoscale Kirkendall effect, (4) structural changes that occur during chemical transformation, (5) structural comparison between nanoparticles and bulk materials, and (6) structural effects on magnetic behavior.

Our findings through this study include various structural and behavioral insights into the Co metal to cobalt phosphide transformation reaction. During the transformation from ε-Co to Co_2P, an interesting crossover point was determined for the diffusivities of cobalt and phosphorus: phosphorus is the faster diffusing species in ε-Co, while cobalt is the faster diffusing species in Co_2P. In Co_2P NPs the Co–Co coordination remains higher than expected due to retention of a cobalt-rich core. The transformation process from Co_2P to CoP is different from that of ε-Co to Co_2P. Theoretical calculations predicted no further hollowing for this transformation, but excess Co in real samples led to further Kirkendall hollowing. The information obtained from this study of nanoparticle transformation from cobalt to cobalt phosphide provides a means to improve synthesis techniques as well as provide insight into the control of structural and magnetic properties, in order to optimize the nanoparticles for use in applications.

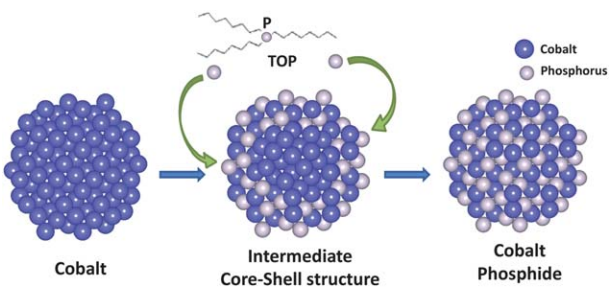

Fig. 1 The evolutional schematics of transition from cobalt to cobalt phosphide nanocrystals.

Methods

Synthesis

All synthesis was carried out in a dry, oxygen-free, di-nitrogen atmosphere by employing standard Schlenk line and glove box techniques. Acetone (≥99.5%), hexanes (≥98.5%), ethanol (≥99.5%), oleic acid (99%), tri-n-octylphosphine oxide (TOPO, 99%), oleylamine (70%), 1,2-dichlorobenzene (99%, anhydrous) and 1-octadecene (90%) were purchased from Aldrich. Tri-n-octylphosphine (TOP, 97%) and $Co_2(CO)_8$ were purchased from Strem Chemicals and Alfa Aesar respectively. Six samples were produced at distinct stages throughout the chemical

transformation of Co metal into Co_2P and CoP. The samples are labeled from **A** to **F**, with **A** corresponding to ε-Co metal, **B** to **E** corresponding to intermediate structures and **F** corresponding to CoP (as determined through XRD). Details of the synthesis are as follows.

The synthesis of ε-Co NPs (sample **A**) followed standard procedures.[38] A N_2 fluxed flask was filled with TOPO (0.1 g). After adding 0.09 g (0.32 mmol) of oleic acid, which is used as a surfactant, dissolved in 12 mL of 1,2-dichlorobenzene, the solution was heated. When the temperature of the solution reached 180 °C, 0.52 g (1.52 mmol) of $Co_2(CO)_8$ dissolved in 4 mL of 1,2-dichlorobenzene was quickly injected. After the reaction progressed for 4 min, the heating mantle was removed and the reaction solution was cooled down in a water bath. The Co NPs were purified by adding ethanol and centrifuged. The supernatant was removed, and the NPs were redispersed in hexanes. The precipitation/redispersion process was performed twice overall.

To synthesize the intermediate phases and Co_2P NPs (samples **B–E**) a flask which was vacuumed and fluxed with N_2, was filled with 12 mL of 1-octadecene and 3 mL of tri-n-octylphosphine. After the solution was heated up to 300 °C, the pre-synthesized ε-Co NPs (~150 mg) dispersed in the mixture of 3 mL 1-octadecene and 3 mL oleylamine were quickly injected into the solution and the reaction proceeded for varied amounts of time, as described in Table 1. The solution was cooled to room temperature by removal of the heating mantle. The NPs were separated by centrifugation and washed twice with acetone/hexanes.

In order to prepare the CoP phase (sample **F**), slightly more aggressive reaction conditions compared to previous samples were necessary.[39] A mixture of ε-Co NPs (~150 mg), 15 mL TOP, and 6 mL oleylamine was heated to 350 °C and kept for 2.5 h. The solution was cooled to room temperature by removal of the heating mantle. The NPs were separated by centrifugation and washed twice with acetone/hexanes.

Nanoparticles were characterized by conventional and high-resolution TEM, X-ray powder diffraction (XRD), EXAFS, and SQUID magnetometry. The conventional TEM images were recorded on an FEI Tecnai T12 operating at 120 kV; the high-resolution TEM images were collected on an FEI Tecnai F20 operating at 200 kV. For statistical analysis at least 200 particles were analyzed. XRD data was collected on a Scintag Theta-Theta X-ray diffractometer (Cu Kα radiation).

XAS spectra of the Co K-edge were obtained using the C-line station at the Cornell High Energy Synchrotron Source (CHESS) using a Si(111) monochromator over an energy range of 7.68–8.20 keV. The nanoparticle samples were diluted to a concentration of 25 mM suspended in toluene, and placed in a 2 mm diameter cylindrical quartz capillary. The spectra were obtained using a four-element fluorescence detector, calibrated with a Co metal foil. An Fe filter was used to control the signal level. For each sample, a minimum of 16 scans at 4 spectra/scan over these 16 scans were averaged for the accuracy of the results, accommodating outliers. Self-absorption was not a concern with the fluorescence detection because the samples were sufficiently dilute in solution at 25 mM. Also, the absorption length of cobalt at 7.7 keV is on a μm scale, which is much larger than the particle size. The fluorescence measurements were proportional to the absorption coefficient, μ(E), which produces a spectrum which describes the strength of X-ray absorption as a function of energy.[13]

Table 1 The reaction conditions of the samples **B–F**

	B	**C**	**D** (Co_2P)	**E**	**F** (CoP)
Reaction time	7 min	10 mins	1 h	2 h	2.5 h
T (°C)	300	300	300	300	350
TOP (mL)	3	3	3	3	15
Oleylamine (mL)	3	3	3	3	6
1-Octadecene (mL)	15	15	15	15	

The raw spectra were averaged and processed using the ATHENA software.[40] This processing included edge determination from the first inflection point in the absorption data, background subtraction using the AUTOBK algorithm, and normalization of the EXAFS modulations (greater than 150 eV above the edge).[41] A k-weight of 1 was chosen for both the Fourier transform (FT) of the experimental data and the theoretical fitting because phosphorus and oxygen are low-Z scattering elements which will scatter mainly at lower k-values.[42] Also, use of a higher k-weight did not compensate for the damping in amplitude due to the high variations in absorber-scatterer distance characteristically observed in nanoparticle spectra.[24] Additionally, as fitting was performed only to the first coordination shell, there was no need to use a higher k-weighting to emphasize high k behavior.[13] The spectra were converted from E-space, to k-space, and then Fourier transformed, according to standard procedure[13] and fitted to theory (see ESI†).[14] In the FT spectrum, peaks appear at the real space position related to a particular shell from the absorbing atom.[43] A phase shift was applied by adding the appropriate pair of known phase shifts of the absorbing and backscattering atom (Co and Co or P respectively).

The data, after processing, were then analyzed by the *ab initio* method with ARTEMIS.[40] Crystal structures from theory were input using ATOMS.[44] Fitting well-matched theoretical pathways to the experimental spectra by allowing structural parameters to deviate from the theoretical bulk structures, specific structural information could be determined such as coordination number, spacing, and mean-square disorder, in accordance with the EXAFS equation[14,43,45,46]

$$\chi(k) = \sum_{\Gamma}\left[\frac{N_\Gamma S_0^2 F_\Gamma(k)}{2kR_\Gamma^2} e^{-2k^2\sigma_\Gamma^2} e^{-2R_\Gamma/\lambda(k)} \times \sin(2kR_\Gamma + \phi_\Gamma(k))\right] \quad (1)$$

Equation (1) above describes the parameters that comprise the EXAFS model. Knowledge of particular parameters enables the determination of others. Γ counts the individual scattering pathways that are summed over. Parameter k is the photoelectron wavevector. $F_\Gamma(k)$, the scattering amplitude, and $\lambda(k)$, the mean free path of inelastically-scattered photoelectrons which contribute to the reduction of the scattering amplitude, are computed by the analysis program. The phase shift $\phi_\Gamma(k)$ is a function of the absorbing and scattering atom and takes into account the fact that the electron is in the presence of potentials.[43] The amplitude reduction factor, S_0^2, theoretically accepted

to be between 0.7 and 1 was set to 0.85 for purposes of extracting the coordination number.[45] The parameters allowed to float during fitting were degeneracy N_Γ, which represents the number of atoms at the same distance from the absorbing atom, R_Γ, the effective distance from the absorbing atom to the scattering atom, and σ^2_Γ, the mean square disorder, which includes components from structural disorder as well as thermal disorder (Debye–Waller factor).[43]

Calculation of diffusion activation barriers

Diffusion activation barriers were calculated as

$$E^{diffusion\ activation} = E^f + E^{barrier} \quad (2)$$

where E^f is the formation energy of the cell including the defect, and $E^{barrier}$ is the energy barrier to migration of the diffusing species, calculated using the nudged elastic band (NEB) method. Formation energies and migration barriers were calculated using the density functional theory (DFT) within the VASP code[47] using the PAW method[48] to describe the core electrons of Co and P and the PBE exchange correlation functional.[49] Further details are given below.

An ε-Co cell which included a single vacancy defect was created by removing either a type I or type II Co atom from the 20-atom ε-Co cell (see ESI† for detailed structure information). Formation energies for the vacancy defects were calculated as

$$E^f_{V(A)} = E\left[\varepsilon\text{-}Co_{19}V(A)\right] - \frac{19}{20}E[\varepsilon\text{-}Co_{20}] \quad (3)$$

where E[ε-Co_{20}] denotes the total energy of the 20-atom ε-Co cell, and E[ε-Co_{19}V(A)] denotes the total energy of the same cell including a vacancy on a site of type A = I or II. The calculated formation energies are $E^f_{\varepsilon-Co_{19}V(I)} = 1.34$ eV and $E^f_{\varepsilon-Co_{19}V(II)} = 1.79$ eV. Since the formation energy of vacancies in type I sites is significantly lower than that for type II sites, only diffusion of Co through type I sites was considered. Note that the type I sublattice forms a network of nearest neighbor sites such that it is possible for an atom to diffuse through an entire crystal of ε-Co on the type I site sublattice.

The barrier to migration of Co atoms from a type I site to a neighboring type I vacancy $E^{barrier}_{Co(I)\leftrightarrow V(I)}$ was calculated using the NEB method. Initial atomic coordinates used for the images in the NEB calculation were generated by linearly interpolating between those of the endpoints. The total activation barrier for Co atoms through vacant type I sites was calculated as

$$E^{diffusion\ activation}_{Co(I)\leftrightarrow V(I)} = E^f_{V(I)} + E^{barrier}_{Co(I)\leftrightarrow V(I)} \quad (4)$$

This value was calculated as $E^{diffusion\ activation}_{Co(I)\leftrightarrow V(I)} = 1.40$ eV.

P atoms can diffuse through the ε-Co crystal through either a substitutional or interstitial mechanism. Considering first substitutional defects, the formation energy for an ε-Co cell including a P atom substituted for a type I Co atom was calculated as $E^f_{P(I)} = -1.00$ eV compared to $E^f_{P(II)} = -0.37$ eV for type II substitution. Since the formation energy $E^f_{P(I)}$ is significantly lower than $E^f_{P(II)}$, only diffusion of P through type I Co sites was considered. An ε-Co cell including both a single vacancy at a type I site, and a P atom substituted for a type I Co atom (which neighbors the vacancy) was created. The formation energy of this cell was calculated as

$$E^f_{V(I)P(I)} = E\left[\varepsilon\text{-}Co_{18}V(I)P(I)\right] - \frac{18}{20}E[\varepsilon\text{-}Co_{20}] - \frac{1}{4}E[b\text{-}P_4] \quad (5)$$

where E[b-P_4] denotes the reference energy of a cell of black phosphorus (used to provide a reference chemical potential for P in our calculations), containing four P atoms. With the barrier to migration calculated in the same way as described for Co diffusion, the total diffusion activation barrier for P atoms through vacant type I sites was found to be $E^{diffusion\ activation}_{P(I)\leftrightarrow V(I)} = 0.58$ eV.

A number of interstitial P sites within the ε-Co cell were attempted, in order to find favorable interstitial defects. The most favorable site attempted for the P atom for the ε-Co_{20} cell is given by the fractional coordinates (0.375, 0.375, 0.375). Symmetry equivalent positions within the cell are given by the fractional coordinates (0.875, 0.125, 0.625), (0.625, 0.875, 0.125), and (0.125, 0.625, 0.875). The formation energy for a ε-Co_{20} cell containing an interstitial P defect at this position is given by

$$E^f_{P(int)} = E[\varepsilon\text{-}Co_{20}P(int)] - E[\varepsilon\text{-}Co_{20}] - \frac{1}{4}E[b\text{-}P_4] \quad (6)$$

The NEB method was used to calculate the barrier to migration between adjacent interstitial sites within the ε-Co_{20} cell, and the total diffusion activation barrier for P atoms through interstitial sites was found to be $E^{diffusion\ activation}_{P(int)\leftrightarrow P(int)} = 1.97$ eV.

The diffusion of Co and P atoms in Co_2P was also investigated. Firstly a Co_2P structure containing a vacancy defect was created; this was achieved by the removal of one of the four type I-Co_2P Co atoms, or of one of the four type II-Co_2P atoms from a Co_8P_4 cell. The defect formation energies relative to that of the Co_2P structure are $E^f_{Co_7P_4V(I-Co_2P)} - E^f_{Co_2P} = 0.55$ eV, and $E^f_{Co_7P_4V(II-Co_2P)} - E^f_{Co_2P} = 0.65$ eV, hence only diffusion of Co through type I-Co_2P sites was considered. The barrier to migration of the Co atom was calculated using the NEB method; the total diffusion activation barrier for Co through type I-Co_2P sites was found to be $E^{diffusion\ activation}_{Co(I-Co_2P)\leftrightarrow V(I-Co_2P)} = 2.24$ eV.

The diffusion activation barrier for P in Co_2P was calculated in a similar way. A P atom was removed from the Co_8P_4 cell to create a vacancy; the barrier to migration of a neighboring P atom into the vacancy was calculated using the NEB method. The diffusion activation barrier for P in Co_2P was found to be 5.80 eV.

Results

TEM was used to characterize the nanoparticle morphology through the phase transformations (Fig. 2A–F and ESI†, Fig. S2). The ε-cobalt nanoparticles of sample **A** are monodisperse in shape and size (11.9 nm, std. dev. 8%) with a spherical morphology (Fig. 2A). Such particle monodispersity is particularly important for EXAFS analysis, which gives insight into average structure.[43] The NPs in sample **B** increase slightly in size and dispersity (12.4 nm, std. dev. 10%) but retain the similar spherical morphology of **A** (Fig. 2B). The nanoparticles of sample **C** further increase in size and dispersity (13.1 nm, std. dev. 12%), and begin to transform into polyhedrons of irregular shape (Fig. 2C). Some of the particles (*ca.* 10%) in sample **C** show

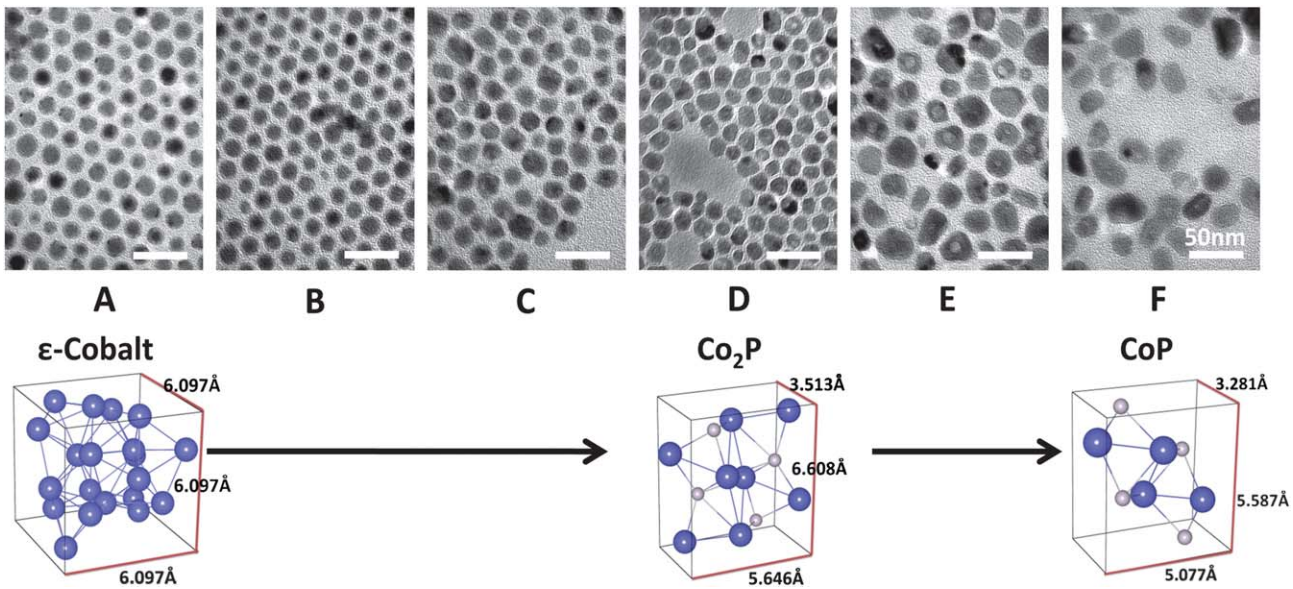

Fig. 2 TEM images of the samples **A–F** (top) and corresponding crystal structures (bottom). The crystal structures shown at bottom (left to right ε-Co, Co_2P and CoP) correspond to sample **A**, **D**, and **F** respectively, as determined from XRD. All scale bars are 50 nm. The larger blue atoms correspond to cobalt, the smaller gray atoms are phosphorus.

a darker core, indicating the onset of the nanoscale Kirkendall effect. The Kirkendall effect arises from the asymmetric diffusivities of atoms and ions in a material.[2] A dark center is commonly seen at the onset of Kirkendall structural hollowing within the nanoparticle core, after transformation is initiated and a shell begins to develop.[2,50] Completely hollow structures are observed in sample **D** (*ca.* 70% of the NPs are hollow with hole size 3.5 nm, std. dev. 17%) as the Kirkendall effect proceeds (Fig. 2D). The NP size distribution of sample **D** increases (12.8 nm, std. dev. 16%). Sample **E** shows an increase in the average nanoparticle size and dispersity (15.7 nm, std. dev. 20%) (Fig. 2E). Additionally, only about 30% of the nanoparticles in **E** show hollow structure and there is an increase in the average size of hollow voids (5.5 nm, std. dev. 32%). Finally, sample **F** shows a slight size increase from sample **E** (16.2 nm, std. dev. 20%) (Fig. 2F). However, only some of **F** (*ca.* 20%) show clear hollow voids. The average size of voids decreases from sample **E** to sample **F** (void size for **F** ~4 nm, std. dev. 24%).[51] This morphological difference between samples **E** and **F** might be the consequence of different reaction conditions: sample **F** is synthesized at a higher temperature for a longer time so it is possible that an annealing of the particle occurred, or the slightly modified reaction conditions for sample **F** favored smaller void formation. Fig. 2 shows the TEM images of these particles with corresponding unit cells for the three distinct phases as determined by XRD (see ESI†, Fig. S1 for the summary of the results).

XRD (Fig. 3) data show a phase transformation from pure Co metal to two different cobalt phosphide phases (Co_2P and CoP). Sample **A** shows ε-Co, which is the phase of Co metal most commonly reported for nanoparticles (Fig. 3, spectrum A).[38,52] The XRD pattern of sample **B** shows the ε-Co phase still present as the majority phase (Fig. 3, spectrum B). The pattern of sample **C** shows a dramatic transition from **B**; there is a strong peak at 41°, and two additional peaks at 52° and 56° (Fig. 3, spectrum C). These peaks correspond to the Co_2P phase. The intensities of these peaks are dominant in the spectrum indicating that Co_2P is the majority phase. A small presence of ε-Co crystal remains in sample **C**, but the strongest peak of ε-Co at 44.6° (seen clearly in samples **A** and **B**) is decreased significantly and the ε-Co peaks at 47.1° and 49.6° also are greatly diminished.

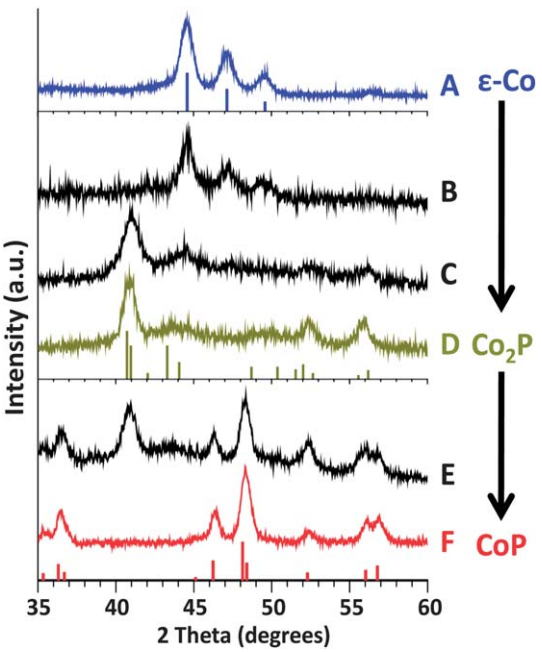

Fig. 3 X-Ray diffraction patterns of samples from **A** to **F**. ε-Co, Co_2P and CoP crystal phases matched well with samples **A**, **D**, and **F** respectively. Stick patterns of ε-Co, Co_2P and CoP are from reference 52, PDF 89-3030, and PDF 29-0497 respectively

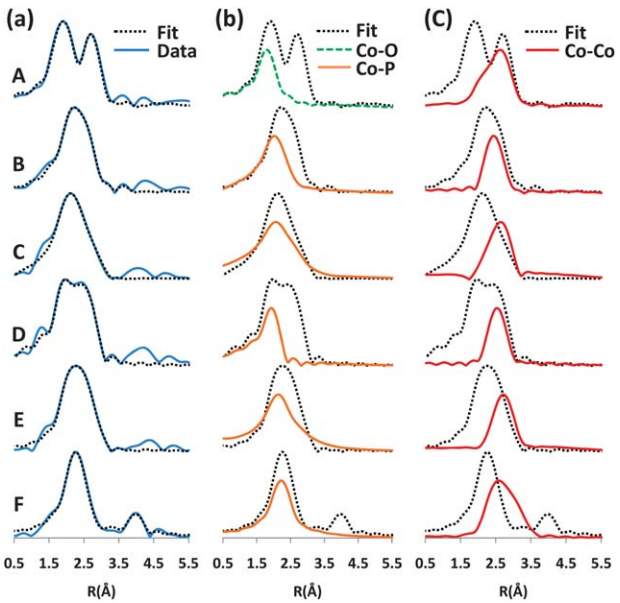

Fig. 4 Fourier-transformed *k*-weighted EXAFS data and simulated fitting results for samples **A–F**. (a) Co K-edge FT-EXAFS experimental data (blue) and first-shell fitting results (dotted black). (b) First-shell fitting (dotted black) and the contributions of the Co–O (dashed green) and Co–P (orange) pathways. (c) First-shell fitting (dotted black) and the contributions of the Co–Co (red) pathways. The sums are normalized path contributions. The intensities of the Co–O, Co–P, and Co–Co contributions are scaled for convenient viewing and do not represent absolute intensities. Vertical axis is FT magnitude in arbitrary units. The Co–Co and Co–P pathways can be again broken down into contributions from the ε-Co, Co_2P, and CoP phases (not shown here: ESI†).

The broadness of the peak at 44.6° is attributed to overlapping of the contribution from both ε-Co and Co_2P. The XRD pattern of **D** shows a crystalline Co_2P phase with no evidence of any other crystal phases (Fig. 3, spectrum D). Also, new Co_2P peaks emerge at higher 2θ in sample **D** which are very weak in sample **C**, indicating the improved crystallinity. The XRD pattern of sample **E** exhibits a mixture of Co_2P and CoP phase (Fig. 3, spectrum E). Unlike the two other intermediate samples **B** and **C**, which do not show well-ordered crystallinity, the intensities of the peaks are stronger in sample **E**, indicating there is a mixture of relatively well-ordered Co_2P and CoP crystalline phases. The XRD spectrum of sample **F** confirms that its phase is CoP with well-defined crystalline order (Fig. 3, spectrum F).

Co K-edge EXAFS was used to investigate the local atomic radial structure around a central cobalt atom through the ε-Co to Co_2P and CoP chemical phase transformation. Only fitting to the first coordination shell (first peak in the FT spectrum, shown in Fig. 4) was performed due to the sharp decrease in the EXAFS amplitude for second and higher order shells because of increased disorder in addition to the presence of low-Z scatterers.[13] Qualitative changes in the overall first shell FT spectrum for the transformation are as follows (Fig. 4a): (1) the first shell peak evolves from a doublet in sample **A**, to an asymmetric singlet in **B** and **C**; (2) two small peaks appear in sample **D** but the doublet is less defined than that of sample **A**; (3) the peaks merge into one broad peak in sample **E**; and (4) the peak is sharpened in sample **F** with a significant second shell contribution.

Table 2 The sum of experimental path degeneracies (coordination number)

	Co–Co		Co–P	
	Results	Bulk theoretical value	Results	Bulk theoretical value
A	11.1	12		
B	10.2		3.4	
C	10.2		4.4	
D	9.9	9	4.7	4.5
E	8.1		5.9	
F	7.5	6	5.5	6

The EXAFS spectrum from sample **A** displays two distinct peaks. The first strong peak at a short distance is attributed to cobalt-oxygen bonding (Fig. 4b, spectrum A). Cobalt oxide is known to form on the surface of Co metal nanoparticles directly after synthesis, and has previously been found on the surface of ε-Co NPs.[24,52,53] Since cobalt oxide is not evident in the XRD spectrum of **A** it may exist as only a few monolayers with amorphous or polycrystalline order. From our experimental EXAFS fittings, the degeneracy of the cobalt-oxygen path is 0.98. This value can be compared to the bulk value of 6 (Table 2 and 3). The degeneracy value is a quantitative measure of the average multiplicity for an individual scattering path. Since the value found here is about 1/6 of the bulk value, it indicates that fewer oxygen atoms are located around the cobalt, on average. The concentration of the atoms on the surface can be calculated by a simple model.[54] Based on the model, the fraction of the atoms on the surface compared to the total number of atoms in one of our 11.9 nm ε-Co NPs is approximately 9% (see ESI†). When we consider the degeneracy of Co–O in our NPs which is 1/6 (~0.17) of bulk, this equals approximately two unit cell layers of cobalt oxide on the surface. These results support the argument that only a few atomic layers become oxidized.

Significant atomic change is apparent between the EXAFS spectra of samples **A** and **B**. Through first-shell fittings (Fig. 4 and Table 3) we are able to assign the doublet peaks in **A** to a Co–O contribution with a shorter bonding distance and Co–Co. Two distinct peaks in sample **A** around 1.9 Å and 2.7 Å merge into one broad peak with a small shoulder and longer radial distance in sample **B**. In sample **B** we are able to deconvolve this asymmetric single peak into contributions from Co–P and Co–Co bonds with shorter and longer bond lengths, respectively. If we include the cobalt-oxygen scattering pathway into the fit for sample **B** a more accurate fit is not achieved, implying that the cobalt-oxygen bonds are removed during the reaction of TOP with the nanoparticle surface.

In sample **C**, Co_2P is the majority phase detected from the XRD pattern with minor contributions from ε-Co metal, but fittings of the EXAFS data show that there is significant ε-Co metal remaining (Fig. 4b, c spectrum C, ESI†, and Table 3). We determine that there is significant ε-Co present by comparing the experimental Co–Co degeneracy and R spacing values to those in the ε-Co and Co_2P theoretical structures. Our experimental Co–Co degeneracy (10.2) is much higher than theoretical values of Co_2P (9). We are able to distinguish Co–Co contributions from ε-Co and Co_2P because the Co–Co average interatomic distance from ε-Co metal (our experimental value: 2.54 Å,

Table 3 Co K-Edge EXAFS structure fitting parameters of samples **A–F**

Sample	Path[a]	N[b]	ΔE_0 (eV)	ΔR (Å)[c]	σ^2 ($\times 10^{-3}$ Å^2)
A	Co_I–Co_I	1.12	8.31	−0.14	15.0
	Co_I–Co_{II}/Co_{II}–Co_I	7.73	9.99	0.02	17.3
	Co_{II}–Co_{II}	2.23	−7.01	0.04	11.8
	Co–O	0.98	−8.74	−0.23	2.1
B	Co_I–Co	4.32	−4.66	0.14	9.9
	Co_{II}–Co	5.88	6.90	−0.02	9.1
	Co_A–P	2.45	−8.96	−0.16	7.4
	Co_B–P	0.96	−9.99	0.02	11.5
C	Co_A–P	3.33	−10	−0.15	11.9
	Co_B–P	1.08	−7.47	−0.07	5.8
	Co_A–Co	7.30	−1.27	−0.02	12.7
	Co_B–Co	2.85	−5.79	−0.16	6.1
D	Co_A–P	2.83	−10	−0.11	10.5
	Co_B–P	1.84	−6.44	−0.07	2.7
	Co_A–Co	6.30	−1.55	−0.08	5.4
	Co_B–Co	3.59	−4.12	−0.03	23.7
E	Co_A–P	3.08	−10	−0.09	17.3
	Co_B–P	2.84	−2.55	−0.02	6.9
	Co_A–Co	4.90	1.59	−0.06	20.0
	Co_B–Co	3.19	−0.64	0.02	12.4
F	Co–P shell 1	5.52	−3.03	−0.04	8.6
	Co–Co shell 1	7.52	−6.49	−0.13	10.0
	Co–P shell 2	8.48	5.08	−0.06	3.8
	Co–Co shell 2	2.46	1.45	0.05	3.0

[a] I and II correspond to type I and II in ε-Co and A and B correspond to type I and II in Co_2P. [b] Reasonable estimates of the errors are ±10%.[16,66] [c] Reasonable estimates of the errors are ±0.01 Å.[66]

theoretical value: 2.51 Å) is shorter than that from Co_2P (our experimental value: 2.67 Å, theoretical value: 2.70 Å). The EXAFS and XRD data imply that the remaining ε-Co metal in sample **C** is composed of very small crystalline domains. The ε-Co core starts as a single crystal. It is unlikely that the remaining metal core is being transformed into a polycrystalline form. Most likely, the ε-Co metal has been reduced in size to only a very small domain.

The EXAFS data show a clear transition from sample **C** to **D**; sample **D** shows two peaks which correspond to the two distinct interatomic pathways, Co–P at 2.26 Å and Co–Co at 2.67 Å, while the EXAFS data only shows one peak for sample **C** (Fig. 4, spectra C and D). As shown in total sums of pathways for Co–P (Fig. 4b, spectra C and D), the Co–P contribution in sample **D** is narrower than in **C** implying more uniform Co–P distances in sample **D**, which is characteristic of a crystal. (Broad peaks generally indicate that atoms are not well organized into exact crystal positions.)[55] The coordination number (CN) of cobalt to phosphorus is lower in sample **C** than in sample **D** (4.4 in **C** *vs.* 4.7 in **D**, Table 2). The bulk value for coordination in Co_2P is 4.5. The slightly higher CN for **D** could imply a thin shell of phosphorus-rich cobalt phosphide on the surface. The high crystalline order of sample **D** provides two distinct, narrow peaks from Co–P and Co–Co pathways in the EXAFS spectrum, which is not the case for the Co–P pathways in intermediate phases **B** and **C** (compare Fig. 4b spectra B, C, D and Fig. 4c spectra B, C, D), nor the Co–Co pathways in sample **C**, with increased deviation from the ε-Co structure. The narrowness of the peaks from both contributions in sample **D** implies that the interatomic distances are well organized which results in a well ordered crystallinity, as a favorable stoichiometric ratio is reached. The EXAFS and XRD data confirm that sample **D** is a converted, well-ordered phase of Co_2P. Despite the increased order within the structure, and pure Co_2P phase shown from XRD results, EXAFS data reveal excess cobalt (experimental CN: 9.9 *vs.* theoretical CN: 9). This may be a result of retention of a Co-rich core, resulting in a particle that, although more well-ordered than intermediate samples **B** and **C**, still lacks a perfect crystalline Co_2P structure.

The EXAFS data for sample **E** reveal a broad distribution of Co–P bonds, similar to that seen in the intermediate sample **C** (Fig. 4b, spectrum E). The Co–P and Co–Co interatomic distances of sample **E** (2.28 Å and 2.69 Å respectively) are slightly larger than those of sample **D** (2.26 Å and 2.67 Å respectively). The overall shape is a single, broad peak centered roughly between the two peaks of sample **D**. The shape change of the peak from sample **D** to **E** (two peaks to one peak) shows the change in atomic positions, which overlap over a broad distribution instead of forming two distinct contributions. Such a change in distribution indicates a decrease in ordered crystallinity[55] in **E** compared to sample **D**, despite the fact that the average length of both Co–P and Co–Co increased.

XRD data show that sample **F** is fully converted to CoP. However, EXAFS results indicate that the sample has more cobalt than that of a perfect CoP phase. The average sum of path degeneracies (CN) of Co–P and Co–Co in sample **F** are 5.5 and 7.5, respectively, while the theoretical bulk values for both are 6

(Table 2). Even when we take into account the ~10% error in the degeneracy value, the Co–Co coordination is higher than that of perfect CoP crystal. This indicates that there is a small excess of Co–Co bonds with short range order that cannot be detected by XRD. Nevertheless, this sample has the best crystallinity of all the samples, evident in the 2nd shell peak in the EXAFS data which is indicative of long range order (Fig. 4a, spectrum F).[13] The superior crystallinity is likely because the reaction was carried out for a longer time and at a higher temperature than the other reactions, leading to conditions more favorable for crystal formation. This well-defined crystallinity present in sample **F** results in a sharp first shell EXAFS peak and well defined second shell peak. This sample has the largest NP size among the samples, which corresponds to more bulk-like behavior with greater long range order.

In order to further explore structural evolution, the EXAFS spectrum for each sample was analyzed for changes in radial structure. The average interatomic distances for Co–P and Co–Co were calculated from the EXAFS data by examining an average of the path distances experimentally found to compose the structures and examining their deviation from bulk/standard distances (see ESI†). Such data reveal the general trends in interatomic spacing as the transformation progresses. An interesting result emerges: the Co–Co distances gradually increase from sample **A** to **F** while those of Co–P stay relatively constant. These results indicate that the interatomic distances between cobalt atoms are lengthened by introducing phosphorus atoms into the system. The Co–Co bond lengths reflect those of bulk materials, as the Co–Co spacings in CoP are longer on average than those of Co_2P, which are longer than those of ε-Co. It appears that the Co–P bonds form at energetically stable distances initially, even as additional phosphorus atoms diffuse into the system, and remained fixed in their positions, resulting in a constant average interatomic distance for Co–P pathways.

The average degeneracies of the Co–Co and Co–P scattering pathways present in the nanoparticle samples and those expected for bulk materials are plotted in Fig. 5. The overall trend of the Co–Co and Co–P coordination mirrors that observed in bulk materials: the Co–Co coordination decreases gradually and the Co–P increases gradually, as the reaction continues to transform from Co metal into Co_2P and then CoP. The slight deviation between NPs and bulk materials for sample **A** (Fig. 5) may be attributed to the surface oxidation of the cobalt NPs, and also for the decrease in coordination as a result of the large number of surface atoms.[56,57] For samples **D** and **F**, some parts of the NPs may contain an amorphous Co-rich region due to the faster outward diffusion of cobalt, resulting in greater cobalt coordination than expected stoichiometrically. Additionally, the mean square disorder term is overall significantly higher than that expected for cobalt bonding in bulk structure ($\sigma^2 \sim 0.003$ Å^2) (see Table 3).[58] This is an observation typically seen in nanoparticles, whose bonds reveal a greater amount of structural disorder due to surface defects.[24,58] This is likely a result of large spreads in interatomic distances compared to bulk structure, which are observed also from the FTs of the spectral data (particularly for intermediate phases). It is also possible that thermal disorder, which increases with higher values of k is contributing to this increase in addition to the greater characteristic structural disorder which our spectral data support. R-factor values between 0.0002 and 0.0082 for each of the theoretical fittings as well as ΔE_0, which represents energy shift,[13,41] values within 10 eV support data reliability (see ESI† and Table 3).

Magnetic results

The transition in magnetic properties from sample **A** to **F** was analyzed by utilizing a superconducting quantum interference device (SQUID, Quantum Design MPMS-XL). Fig. 6 shows magnetic hysteresis loops of samples measured at 2 K. Sample **A** shows ferromagnetic behavior, with a coercivity of 1800 Oe. There is a significant coercivity drop observed in sample **B** compared to **A** (~280 Oe). Even though the major phase of sample **B** is ε-Co from XRD, the ferromagnetic behavior was suppressed greatly which indicates the magnetic properties are sensitive. A gradual decrease in ferromagnetic behavior was shown in sample **C** (coercivity ~ 200 Oe). Samples **D** and **F** showed paramagnetic behavior which corresponds to the behavior characteristic to bulk Co_2P and CoP, which are both known as paramagnetic materials.[59] Sample **E** which is an

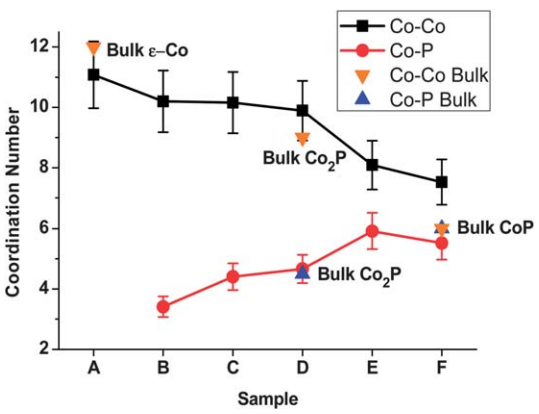

Fig. 5 The coordination numbers of Co–Co and Co–P from the fitting results and those of bulk theoretical values. Labels have been added to clarify the bulk phases (*e.g.*, At sample **A** Co–Co bonding corresponds to that in ε-Co phase). Reasonable estimates of the errors are ±10%[16,66]

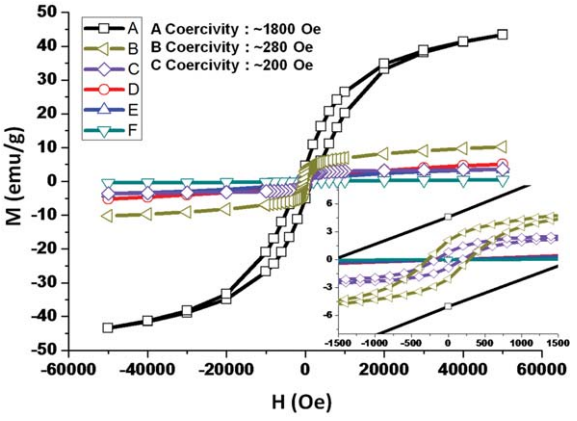

Fig. 6 The magnetic hysteresis loops of the samples at 2 K. The hysteresis loops gradually shrink from sample **A** through **B** to **C**. Coercivities of samples **A**, **B**, and **C** are 1800, 280, and 200 Oe respectively. Samples **D**, **E**, and **F** which are paramagnetic show no hysteresis loop.

Table 4 The formation energy, migration barrier, and diffusion activation barrier for Co and P diffusing through ε-Co

Diffusion type	Formation energy (eV)	Barrier to migration (eV)	Diffusion activation barrier (eV)
Co(I) ↔ V(I)	1.34	0.06	1.40
P(I) ↔ V(I)	0.05	0.53	0.58
P(int) ↔ P(int)	−0.63	2.60	1.97

intermediate sample between samples **D** and **F**, also appeared to be paramagnetic.

Theoretical results

In order to determine the transformation path from ε-Co to Co_2P in the nanoparticle, diffusion activation barriers for Co and P diffusing through vacant sites in bulk ε-Co were determined, as well as the diffusion activation barrier for P diffusing through interstitial sites in bulk ε-Co. Co atoms are more likely to diffuse through type I sites than type II sites, due to the lower formation energy for a vacancy at a type I site. Diffusion of P atoms through type I sites was also found to be favorable; diffusion through interstitial sites was prohibited by the high barrier to migration. Since the lowest diffusion activation barrier calculated was for P atoms through vacant type I sites, P is expected to diffuse more quickly than Co in the ε-Co crystal. Details of the activation barrier calculations are given in the Methods section. Table 4 gives the formation energy, migration barrier, and diffusion activation barrier for Co and P diffusing through ε-Co.

Diffusion activation barriers were also calculated for Co and P through Co_2P. Table 5 gives the formation energy, migration barrier and diffusion activation barrier for Co and P diffusing through vacant sites in Co_2P.

The calculated diffusion activation barriers suggest that P diffuses more quickly than Co through the ε-Co structure, while conversely, Co diffuses faster than P through the Co_2P structure. This shows that the fastest diffusing species switches from P to Co somewhere in between ε-Co and Co_2P. The calculated diffusion activation energy values also suggest that Co diffusion through type I-Co_2P sites is more favorable than P diffusion in Co_2P and type II-Co_2P Co (see Table 5 and Methods section). This has important consequences for the mechanism governing the transformations from ε-Co to Co_2P, and from Co_2P to CoP, which will be discussed in the Discussion section.

Density of states for Co_2P and CoP

Density of states (DOS) calculations were carried out for the Co_2P and CoP phases, using the GGA PBE[49] exchange correlation functional and the hybrid HSE06[60] functional. DOS plots are shown in Fig. S13 in the supporting information. The Fermi level is indicated by the dashed green line in each case. Contrary to a recent experimental study of Co_2P and CoP nanocrystals,[61] the Co_2P and CoP structures are metallic and no band gap is observed for either phase. Semilocal density functionals such as the PBE often underestimate the bandgap and sometimes even predict metallic structures instead of the observed semiconducting phases. However, we confirm the predicted metallic structures using the HSE06 hybrid exchange–correlation functional,[60,62] which has been shown to be highly accurate for the prediction of semiconductor bandgaps.[63]

Table 5 The formation energy, migration barrier and diffusion activation barrier for Co and P diffusing through vacant sites in Co_2P

Diffusion type	Formation energy (eV)	Barrier to migration (eV)	Diffusion activation energy (eV)
Co(I-Co_2P) ↔ V(I-Co_2P)	0.55	1.69	2.24
P ↔ V	2.81	2.99	5.80

Discussion

The ε-Co to Co_2P to CoP chemical transformation was investigated through a combination of TEM, XRD, SQUID, and EXAFS. Defect formation energies and migration barriers were calculated using DFT; the sum of these two quantities gives the full diffusion activation barrier for the defects considered, which may be used to infer the most likely diffusion mechanism during the transformation. To discuss the mechanisms for transformation we divide the transformations into two sections: (I) ε-Co to Co_2P and (II) Co_2P to CoP. We do this in part because the diffusivities change depending on the chemical environment. For example, the cobalt atoms/ions diffuse faster in Co_2P than in ε-Co when reacted with excess phosphorus.

(I) ε-Co to Co_2P

We believe that two steps are involved in the phase transformation from ε-Co to Co_2P. The first step is inward diffusion of phosphorus atoms into ε-Co NPs, forming Co-rich Co_2P. The second step is outward diffusion of Co from a Co_2P compound, leaving a hollow void through the Kirkendall mechanism.

Step 1, inward P diffusion. From our calculations of diffusion activation barriers, the phosphorus atoms diffuse much faster than cobalt atoms in ε-Co (see Table 4). Considering the calculated diffusion activation barriers, diffusion is likely to take place in the ε-Co nanoparticle by P atoms taking vacant type I sites. Despite the lower barrier to migration for Co atoms traveling through type I sites, P atoms will diffuse more quickly due to a lower formation energy for the defect of a P atom/vacancy pair, compared to a vacancy alone. Interstitial P diffusion is ruled out due to the far higher barrier to migration, which is a result of the relatively high density of ε-Co. Therefore, phosphorus atoms diffuse into ε-Co NPs and form a Co_2P phase and/or a Co-rich Co–P phase, while the diffusion of cobalt atoms is not significant. The inward-diffusing P atoms form an amorphous shell of Co–P around the ε-Co core (see Fig. 7), which then transforms to crystalline Co_2P. Our theoretical modeling suggests that an outer shell of Co_2P is formed around the nanoparticle by the inward diffusion of P atoms through a mechanism of substitutional hopping and vacancy formation.

Step 2, outward Co diffusion. However, when the phase approaches crystalline Co_2P, the diffusion mechanism changes, causing the Kirkendall hollowing. From our calculations, in the Co_2P phase the outward diffusion of Co is faster than inward

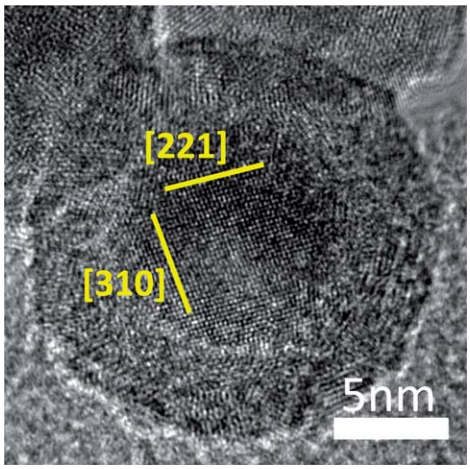

Fig. 7 The HRTEM image of the intermediate NP between ε-Co and Co_2P. The core shows ε-Co phase as indicated by the (221) and (310) lattice planes. The reaction conditions of this sample followed that of sample **B**.

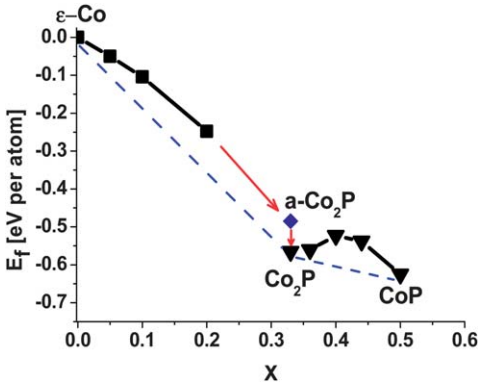

Fig. 8 Formation energy per atom for $Co_{1-x}P_x$ structures illustrating the proposed path between the ε-Co, Co_2P, and CoP structures. The black squares indicate structures in which P atoms have been substituted for type I Co atoms in the ε-Co crystal. The blue diamond indicates an amorphous structure with stoichiometry Co_2P (a- Co_2P), through which the transformation to crystalline Co_2P may take place. The black triangles indicate the proposed path from Co_2P to CoP; for the intermediate structures between one and three type I-Co_2P Co atoms have been removed from the Co_2P cell. The blue dashed tie line connects the stable phases.

diffusion of P (see Table 5). There is a critical point during the phase transition from ε-Co to Co_2P after which the relative diffusivity of Co exceeds that of P atoms. After this point the Kirkendall effect dominates and the Co from the Co-rich core diffuses outward faster than P can diffuse inward, leaving a hollow center.

Experimental data confirms both of these process steps (step 1 and 2). We see that the phosphorus atoms diffuse through the surface of the cobalt NPs, initially replacing the cobalt oxide native layer, and then forming a phosphorus-rich amorphous shell (EXAFS of **A** to **B**). ε-Co crystal is the majority phase while the Co–P shell is forming (XRD of **B**), then ε-Co co-exists with the Co_2P phase (XRD of **C**), and finally the NP transforms into a dominant Co_2P phase, albeit with a higher concentration of Co atoms (XRD and EXAFS of **D**). TEM images of the transformation show a solid core until the dominant phase Co_2P NP, which is hollow (**D**). That is: until the Co_2P phase appears in crystalline form (**C**) there is no void formation, which corresponds well to our theoretical predictions that asymmetric outward diffusion of Co is minimal until a Co_2P phase appears.

In the pre-crystalline Co_2P the core-shell intermediate stage has an amorphous shell and a crystal core, which was characterized by HRTEM and modeled through DFT. HRTEM images of the intermediate stage between ε-cobalt and Co_2P showed NP cores of pure epsilon phase confirmed by analyzing the lattice planes (Fig. 7). The outer shell exhibited poor crystallinity with nearly no lattice planes evident in HRTEM, indicating an amorphous structure. It is possible that this amorphous outer shell layer might be composed of short orderings of the cobalt-phosphorus bonds. These HRTEM results correlate well with the EXAFS results which reveal the presence of Co–P coordination while XRD results show no evidence of cobalt phosphide phases. Theoretical modeling of this shell confirms the experimental observations. DFT calculations of the formation energy of an amorphous structure with stoichiometry Co_2P was −0.49 eV per atom, compared to −0.57 eV per atom for crystalline Co_2P. The relatively low energy of the amorphous phase suggests that the transformation to Co_2P in the nanoparticle shell may take place through the amorphous structure (Fig. 8).

As crystalline Co_2P forms, structural hollowing occurs due to the nanoscale Kirkendall effect (transformation of sample **C** to **D**). The Co_2P crystal must initially form on the outside of the NP sphere since Co metal coexists with the Co_2P phase (XRD of **C**), and HRTEM of previous NPs show a solid core of ε-Co metal. (From our calculations and HRTEM data it is very unlikely that the Co metal diffuses outward as crystalline Co metal clusters. Therefore, the majority of the Co metal is in the core.) Once the Co_2P crystal is formed, the Co atoms in the Co-rich core diffuse out faster than P atoms diffuse in, leaving a void (TEM of **D**, Fig. 2). This is an intriguing finding and suggests that the inner hollow void size could be tuned if the rate of Co_2P crystal formation on the outer shell could be controlled. (For example, one could introduce a limited amount of P into the system and allow a defined shell of Co_2P to form, then introduce more P to instigate Kirkendall hollowing. From our results, one should expect that the initial thickness of the shell of Co_2P will define the void size.)

(II) Co_2P to CoP

Based on the calculation of the diffusion activation barriers of Co and P in Co_2P, the transformation from Co_2P to CoP most likely takes place through the de-intercalation of Co from type I-Co_2P sites, while the connectivity of the anion sublattice remains intact, as shown in Fig. 9. Fig. 9 illustrates a possible path by which ideal Co_2P can transform to CoP: type I-Co_2P Co atoms are successively removed from the initial Co_2P cell. This is consistent with the diffusion of Co atoms out from the center of the nanoparticle towards the surface. This transformation involves a deformation in the shape of the P sublattice, as indicated by the red highlighted bonds in Fig. 9. The anion sublattice retains connectivity, however, which is consistent with what is

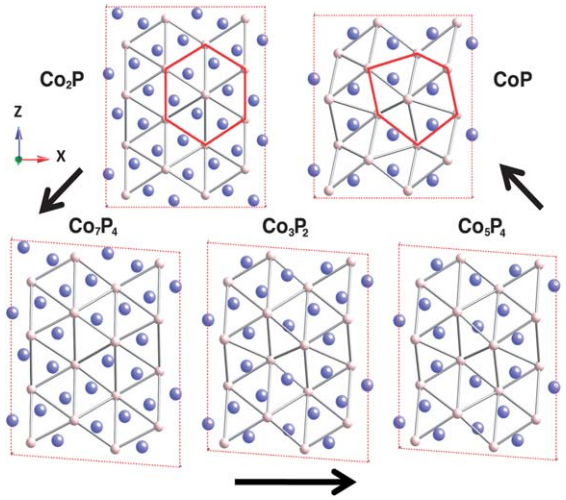

Fig. 9 Supercells illustrating a possible path between the Co_2P and CoP structures are shown, viewed along the [0 1 0] direction. The structure was relaxed using DFT after successively removing type I-Co_2P Co atoms, resulting in a deformation of the P sublattice. After the removal of four Co atoms the CoP structure was achieved. The bonds highlighted in red indicate the P sublattice associated with the Co_2P and CoP structures, which retains connectivity during the transformation.

seen during cation exchange reactions in nanocrystals.[4,5] That is: in an ideal transformation from Co_2P to CoP, no hollowing due to Kirkendall effects would take place; the only shape change would be additional layers of CoP forming at the outer surface of the nanoparticle. However, a nanoparticle containing a Co-rich core and a Co_2P shell would result in Kirkendall hollowing (as detailed in the previous sections) from the center of the nanoparticle, and thus the transformation should result in the creation or enlargement of a pore at the nanoparticle center.

The actual NP samples, however, showed slightly different behavior compared to the theoretical predictions of pure Co_2P, and were more similar to the latter case with a Co-rich core. In the transition from Co_2P (sample **D**) to the interphase Co_2P/CoP (sample **E**) the NPs become more polydisperse, the hollow voids increase in diameter, and the percentage of hollow particles decreases by more than half (from 70% with hollow centers in **D** to 30% in **E**). Clearly more is occurring than the simple shuttling of Co through the anion lattice predicted for perfect crystals. Based on our experimental results we believe in our samples there is (1) a Co-rich inner region which leads to the continued void expansion and (2) a fracturing of hollow particles with leads to the increase in polydispersity and decrease in percentage of hollow particles. Though not mutually exclusive, these two phenomena will create two pathways for the transition from our NP Co_2P to CoP (Fig. 10).[64]

In the first path (Fig. 10 path a) the CoP NPs grow in diameter by diffusion of cobalt atoms from the Co-rich Co_2P interior, forming additional CoP on the surface. This accounts for the void size increase and the increase in overall particle size. The void size *should* remain fixed after the initial ε-Co to Co_2P Kirkendall reaction since the Co_2P to CoP reaction is expected to maintain a structural integrity through the anion sub-lattice (see previous theoretical section). However, our Co_2P NPs (sample **D**) are not perfect Co_2P: EXAFS results show that the

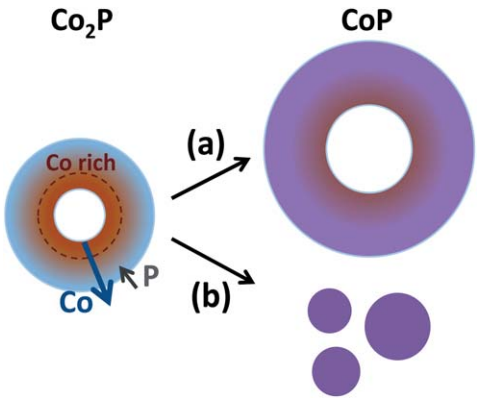

Fig. 10 Two pathways for the transition from the Co_2P to CoP sample. In the Co_2P NP (left), the inner brown region indicates the cobalt rich part. The longer Co arrow symbolizes the larger diffusivity of Co over P (shorter arrow). (a) NPs grow by diffusion of cobalt atoms from inside of NPs to surface. (b) NPs break into smaller particles during the reaction.

degeneracy of the Co–Co coordination (9.9) is higher than that of the theoretical value (9), which means that the concentration of cobalt atoms is higher than a perfect Co_2P crystal. This higher concentration of cobalt atoms should occur as a gradient from the interior to the exterior, with the interior having the highest concentration and the exterior having the lowest. These excess cobalt atoms facilitate a continued Kirkendall effect and result in bigger voids in the intermediate phase between Co_2P and CoP (sample **E**). SQUID and XRD results indicate that metal Co clusters are not present in samples **D–F** so the Co_2P and CoP are Co-rich and *do not* contain a significant amount of Co metal clusters, which should be detected by SQUID.[65]

In the second path for our Co_2P to CoP transformation (Fig. 10 path b) the NPs fracture into smaller pieces during the reaction (Fig. 2D and E). Fracturing of hollow NPs into smaller NPs is commonly seen in hollow NP systems.[2,50] The increase in size deviation in our samples (std. dev. of 16% in **D** to 20% in **E**) is then due to this fracturing since new small NPs are formed that skew the size deviations. The small pieces may then undergo Ostwald ripening as they dissolve and the new material is added to the larger NPs. This would also increase polydispersity and explain the increase in irregular shapes (TEM of sample **E**). The fracturing also explains the decrease in the percentage of hollow NPs (from 70% to 30%) because newly formed small NPs are not hollow.

In sample **F**, with a longer reaction time and higher temperatures, re-annealing is observed for a majority of the nanoparticles, increasing the crystalline order with increased phosphorus diffusion. This resulted in a significant second shell contribution to the EXAFS spectrum which indicates that sample **F** acts as more bulk-like than other samples. It is interesting to note that higher temperatures and longer reaction times lead to such large morphological differences with this sample compared to the others. For instance, hollowing is lessened in these particles compared to the intermediate Co_2P/CoP particles.

Conclusion

A thorough means to elucidate nanoparticle atomic and morphological structure through a chemical transformation is

presented, with the use of X-ray absorption spectroscopy, XRD, TEM, and DFT calculations. Atomic coordination and structural evolution, including diffusion processes, throughout the transformation of NP ε-Co to Co_2P and CoP are reported.

EXAFS and XRD analysis revealed that the NPs which show pure Co_2P and CoP phase in XRD spectra were not perfect structures: the Co–Co coordination number was greater in NPs than in bulk, resulting in a cobalt-rich gradient from the interior to exterior of the NPs.

We propose that the transformation from ε-Co to Co_2P occurs through two sequential diffusion steps: (1) inward diffusion of phosphorus with negligible movement of cobalt and (2) outward diffusion of cobalt which results in a hollow structure. During the first step, cobalt phosphide first forms an amorphous shell layer in the exterior portion of the NP before a complete transformation occurs. When ε-Co is the majority phase the P atoms diffuse inward faster than Co diffuses outward. After the transformation progresses and Co_2P becomes the majority phase in the NPs, the diffusivity of Co exceeds that of P, resulting in outward diffusion of cobalt atoms and the formation of hollow voids as is characteristic of the nanoscale Kirkendall effect.

As Co_2P transforms into CoP a different transformation mechanism is involved. Cobalt atoms de-intercalate from interstitial sites while the anion lattice remains intact. Although theoretical calculations predict no further structural hollowing within the NPs, in the real samples the cobalt-rich interior causes further hollowing. This residual metal has implications for other nanoscale Kirkendall systems and the properties of the resulting compounds. In the final CoP nanoparticle structure, re-annealing occurs, resulting in NPs with long-range order that lack hollow voids.

Our findings provide an elucidation of cobalt to cobalt phosphide NP transformation and structure. Knowledge about the transformation method and structural properties provides a means to fine-tune the synthesis and composition of the NPs and facilitate the optimization of such NPs for use in applications. We predict that it is possible to tailor the void size in Co_2P hollow nanoparticles by varying the initial Co_2P shell size. The Co diffusion through the Co_2P anion lattice is an intriguing mechanism that deserves further study. It may be possible to use CoP for ionic conduction of Co.

Acknowledgements

We thank Ken Finkelstein for his assistance with obtaining data, experimental setup at CHESS and advice concerning data analysis. We also thank the Pollack and Abruña groups for their helpful suggestions for conducting XAS experiments and analysis. We thank Peter Ko for his helpful discussion on EXAFS data analysis. This work was supported in part by Award No. KUS-C1-018-02, made by King Abdullah University of Science and Technology (KAUST). We also acknowledge support of Cornell Center for Materials Research (CCMR) with funding from the Materials Research Science and Engineering Center program of the National Science Foundation (cooperative agreement DMR 0520404), and the support of Energy Materials Center at Cornell (EMC^2), an Energy Frontier Research Center funded by the U.S. Department of Energy, Office of Science, Office of Basic Energy Science under Award Number DE-SC0001086. L.M.M. is supported from the Engineering Learning Initiatives Undergraduate Research Grants Program at Cornell University, with sponsorship from the SRC Education Alliance URO by Intel Foundation.

References

1 A. I. Frenkel, C. W. Hills and R. G. Nuzzo, *J. Phys. Chem. B*, 2001, **105**, 12689–12703.
2 Y. D. Yin, R. M. Rioux, C. K. Erdonmez, S. Hughes, G. A. Somorjai and A. P. Alivisatos, *Science*, 2004, **304**, 711–714.
3 Y. G. Sun and Y. N. Xia, *J. Am. Chem. Soc.*, 2004, **126**, 3892–3901.
4 D. H. Son, S. M. Hughes, Y. D. Yin and A. P. Alivisatos, *Science*, 2004, **306**, 1009–1012.
5 R. D. Robinson, B. Sadtler, D. O. Demchenko, C. K. Erdonmez, L. W. Wang and A. P. Alivisatos, *Science*, 2007, **317**, 355–358.
6 D. O. Demchenko, R. D. Robinson, B. Sadtler, C. K. Erdonmez, A. P. Alivisatos and L. W. Wang, *ACS Nano*, 2008, **2**, 627–636.
7 B. Sadtler, D. O. Demchenko, H. Zheng, S. M. Hughes, M. G. Merkle, U. Dahmen, L. W. Wang and A. P. Alivisatos, *J. Am. Chem. Soc.*, 2009, **131**, 5285–5293.
8 S. E. Wark, C. H. Hsia and D. H. Son, *J. Am. Chem. Soc.*, 2008, **130**, 9550–9555.
9 Z. Y. Tang, N. A. Kotov and M. Giersig, *Science*, 2002, **297**, 237–240.
10 K. S. Cho, D. V. Talapin, W. Gaschler and C. B. Murray, *J. Am. Chem. Soc.*, 2005, **127**, 7140–7147.
11 E. M. Chan, M. A. Marcus, S. Fakra, M. ElNaggar, R. A. Mathies and A. P. Alivisatos, *J. Phys. Chem. A*, 2007, **111**, 12210–12215.
12 A. Frenkel, *Z. Kristallogr.*, 2007, **222**, 605–611.
13 G. Bunker, *Introduction to XAFS: a practical guide to X-ray absorption fine structure spectroscopy*, Cambridge University Press, Cambridge, 2010.
14 E. A. Stern, *Phys. Rev. B: Solid State*, 1974, **10**, 3027–3037.
15 D. M. Aruguete, M. A. Marcus, L. S. Li, A. Williamson, S. Fakra, F. Gygi, G. A. Galli and A. P. Alivisatos, *J. Phys. Chem. C*, 2007, **111**, 75–79.
16 M. A. Marcus, W. Flood, M. Stiegerwald, L. Brus and M. Bawendi, *J. Phys. Chem.*, 1991, **95**, 1572–1576.
17 B. J. Hwang, L. S. Sarma, J. M. Chen, C. H. Chen, S. C. Shih, G. R. Wang, D. G. Liu, J. F. Lee and M. T. Tang, *J. Am. Chem. Soc.*, 2005, **127**, 11140–11145.
18 M. S. Nashner, A. I. Frenkel, D. L. Adler, J. R. Shapley and R. G. Nuzzo, *J. Am. Chem. Soc.*, 1997, **119**, 7760–7771.
19 M. S. Nashner, A. I. Frenkel, D. Somerville, C. W. Hills, J. R. Shapley and R. G. Nuzzo, *J. Am. Chem. Soc.*, 1998, **120**, 8093–8101.
20 A. I. Frenkel, *J. Synchrotron Radiat.*, 1999, **6**, 293–295.
21 J. I. Park, M. G. Kim, Y. W. Jun, J. S. Lee, W. R. Lee and J. Cheon, *J. Am. Chem. Soc.*, 2004, **126**, 9072–9078.
22 L. S. Sarma, C.-H. Chen, S. M. S. Kumar, G.-R. Wang, S.-C. Yen, D.-G. Liu, H.-S. Sheu, K.-L. Yu, M.-T. Tang, J.-F. Lee, C. Bock, K.-H. Chen and B.-J. Hwang, *Langmuir*, 2007, **23**, 5802–5809.
23 J. A. Rodriguez, J. C. Hanson, J. Y. Kim, G. Liu, A. Iglesias-Juez and M. Fernandez-Garcia, *J. Phys. Chem. B*, 2003, **107**, 3535–3543.
24 G. Cheng, J. D. Carter and T. Guo, *Chem. Phys. Lett.*, 2004, **400**, 122–127.
25 J. Rockenberger, L. Troger, A. Kornowski, T. Vossmeyer, A. Eychmuller, J. Feldhaus and H. Weller, *J. Phys. Chem. B*, 1997, **101**, 2691–2701.
26 S. L. Brock, S. C. Perera and K. L. Stamm, *Chem.–Eur. J.*, 2004, **10**, 3364–3371.
27 A. T. Kelly, I. Rusakova, T. Ould-Ely, C. Hofmann, A. Luttge and K. H. Whitmire, *Nano Lett.*, 2007, **7**, 2920–2925.
28 K. A. Gregg, S. C. Perera, G. Lawes, S. Shinozaki and S. L. Brock, *Chem. Mater.*, 2006, **18**, 879–886.
29 Y. Li, M. A. Malik and P. O'Brien, *J. Am. Chem. Soc.*, 2005, **127**, 16020–16021.
30 D. C. S. Souza, V. Pralong, A. J. Jacobson and L. F. Nazar, *Science*, 2002, **296**, 2012–2015.
31 Y. H. Ni, J. Li, L. Jin, J. Xia, J. M. Hong and K. M. Liao, *New J. Chem.*, 2009, **33**, 2055–2059.
32 Y. Ni, J. Li, L. Zhang, S. Yang and X. Wei, *Mater. Res. Bull.*, 2009, **44**, 1166–1172.

33 I. Lucas, L. Perez, C. Aroca, P. Sánchez, E. López and M. C. Sánchez, *J. Magn. Magn. Mater.*, 2005, **290–291**, 1513–1516.
34 A. W. Burns, K. A. Layman, D. H. Bale and M. E. Bussell, *Appl. Catal., A*, 2008, **343**, 68–76.
35 H. Zhang, D.-H. Ha, R. Hovden, L. F. Kourkoutis and R. D. Robinson, *Nano Lett.*, 2011, **11**, 188–197.
36 C. M. Lukehart, S. B. Milne and S. R. Stock, *Chem. Mater.*, 1998, **10**, 903–908.
37 M. E. Schlesinger, *Chem. Rev.*, 2002, **102**, 4267–4301.
38 V. F. Puntes, K. M. Krishnan and A. P. Alivisatos, *Science*, 2001, **291**, 2115–2117.
39 The mixture of Co_2P and CoP was obtained when the reaction continues for 5 h using the same conditions for sample B–E.
40 B. Ravel and M. Newville, *J. Synchrotron Radiat.*, 2005, **12**, 537–541.
41 S. D. Kelly and B. Ravel, *AIP Conf. Proc.*, 2007, **882**, 132–134.
42 D. C. Koningsberger, B. L. Mojet, G. E. van Dorssen and D. E. Ramaker, *Top. Catal.*, 2000, **10**, 143–155.
43 E. A. Stern, *Contemp. Phys.*, 1978, **19**, 289–310.
44 B. Ravel, *J. Synchrotron Radiat.*, 2001, **8**, 314–316.
45 B. Ravel and S. D. Kelly, *AIP Conf. Proc.*, 2007, **882**, 150–152.
46 R. Scott, *Physical Methods in Bioinorganic Chemistry: Spectroscopy and Magnetism*, University Science Books, 2000.
47 G. Kresse and J. Furthmüller, *Phys. Rev. B*, 1996, **54**, 11169.
48 P. E. Blöchl, *Phys. Rev. B*, 1994, **50**, 17953; G. Kresse and D. Joubert, *Phys. Rev. B*, 1999, **59**, 1758.
49 J. P. Perdew, K. Burke and M. Ernzerhof, *Phys. Rev. Lett.*, 1996, **77**, 3865.
50 Y. D. Yin, C. K. Erdonmez, A. Cabot, S. Hughes and A. P. Alivisatos, *Adv. Funct. Mater.*, 2006, **16**, 1389–1399.
51 The average size of hollow voids in sample F is not accurate due to their irregular shapes.
52 D. P. Dinega and M. G. Bawendi, *Angew. Chem., Int. Ed.*, 1999, **38**, 1788–1791.
53 S. Jia, C.-H. Hsia and D. H. Son, *J. Phys. Chem. C*, 2011, **115**, 92–96.
54 R. L. Johnston, *Atomic and Molecular Clusters*, Taylor & Francis, 2002.
55 J. C. Cezar, H. C. N. Tolentino and M. Knobel, *Phys. Rev. B: Condens. Matter*, 2003, **68**, 054404.
56 S. Calvin, C. J. Riedel, E. E. Carpenter, S. A. Morrison, R. M. Stroud and V. G. Harris, *Phys. Scr.*, 2005, **T115**, 744–748.
57 L. X. Chen, T. Rajh, W. Jager, J. Nedeljkovic and M. C. Thurnauer, *J. Synchrotron Radiat.*, 1999, **6**, 445–447.
58 D. J. Sprouster, R. Giulian, L. L. Araujo, P. Kluth, B. Johannessen, D. J. Cookson, G. J. Foran and M. C. Ridgway, *J. Appl. Phys.*, 2010, **107**, 014313–014310.
59 S. Fujii, S. Ishida and S. Asano, *J. Phys. F: Met. Phys.*, 1988, **18**, 971–980.
60 J. Paier, M. Marsman, K. Hummer, G. Kresse, I. C. Gerber and J. G. Angyan, *J. Chem. Phys.*, 2006, **124**, 154709–154713.
61 W. Maneeprakorn, M. A. Malik and P. O'Brien, *J. Mater. Chem.*, 2010, **20**, 2329–2335.
62 J. Heyd, G. E. Scuseria and M. Ernzerhof, *J. Chem. Phys.*, 2003, **118**, 8207–8215.
63 J. Heyd, J. E. Peralta, G. E. Scuseria and R. L. Martin, *J. Chem. Phys.*, 2005, **123**, 174101–174108.
64 This explanation is mainly based on the sample D and E because the synthetic conditions of sample F are slightly different (Table 1).
65 E. Barea, X. Batlle, P. Bourges, A. Corma, V. Fornes, A. Labarta and V. F. Puntes, *J. Am. Chem. Soc.*, 2005, **127**, 18026–18030.
66 R. Nietubyc, E. Czerwosz, R. Diduszko, P. Dluzewski, M. Kozlowski and E. Welter, *J. Alloys Compd.*, 2009, **484**, 896–901.

